PAPER

Absorptive Fabry–Pérot Interference in a Metallic Nanostructure*

Absorptive Fabry–Pérot Interference in a Metallic Nanostructure *

Rui Wang(王瑞)[1], Yan-Ling Wu(吴艳玲)[2], B. H. Yu(余博晗)[2,3], Li-Li Hu(胡立立)[2], C. Z. Gu(顾长志)[2,3], J. J. Li(李俊杰)[2,3], Jimin Zhao(赵继民)[2,3,4]**

[1]*CAS Key Laboratory of Standardization and Measurement for Nanotechnology, CAS Center for Excellence in Nanoscience, National Center for Nanoscience and Technology, Beijing 100190*

[2]*Beijing National Laboratory for Condensed Matter Physics, Institute of Physics, Chinese Academy of Sciences, Beijing 100190*

[3]*School of Physical Sciences, University of Chinese Academy of Sciences, Beijing 100049*

[4]*Songshan Lake Materials Laboratory, Dongguan 523808*

(Received 24 October 2018)

In conventional optics, the Fabry–Pérot (FP) effect is only considered for transparent materials at a macroscopic dimension. Down to the nanometer scale, for absorptive metallic structures, the FP effect has not been directly observed so far. It is unclear whether such a macroscopic effect still holds for a subwavelength metallic nanostructure. Here, we demonstrate the probing of FP interference in a series of nanometer-thick Au films with subwavelength hole arrays. The evidence from both linear and second harmonic generation signals, together with angle-resolved investigations, exhibit features of a FP effect. We also derive an absorptive FP interference equation, which well explains our experimental results. Our results for the first time experimentally confirm the long-persisting hypothesis that the FP effect holds ubiquitously in a metallic nanostructure.

PACS: 78.67.−n, 42.65.−k DOI: 10.1088/0256-307X/36/2/027801

Many novel phenomena occur when light propagates through subwavelength hole arrays in a metallic film, such as extraordinary linear optical transmission[1−6] and unusually enhanced second harmonic generation (SHG).[7−10] It is known that, for these systems, hole shape,[2−4,7,11] hole size,[4] and hole array periodicity[2,12] all play an essential role in light propagation. Among the various optical properties at a subwavelength scale, the Fabry–Pérot (FP) interference effect has been theoretically considered[13] and experimentally investigated in the microwave regime,[14] where a non-plasmon mechanism has been proposed.[15] Nonetheless, these works are not down to a nanometer scale. It is unclear whether the FP interference effect still holds for a metallic nanostructure that is both smaller than the wavelength and strongly absorptive. The FP effect has been used to successfully explain surface plasmon propagation in metal nanowires. However, the sample dimension along the plasmon propagation direction is still larger than the laser wavelength.[16,17] Similar interference effects have also been observed in an above-wavelength airgap.[18] However, a direct observation of the FP effect in a subwavelength metallic nanostructure is still lacking.

In this work, we use ultrafast laser pulses to make thorough quantitative measurements of the thickness-dependence and angle-dependence of the linear transmission and SHG intensity in Au thin films with rectangular subwavelength hole arrays. We observe features of the FP interference effect in both linear and SHG signals. A direct realization of the FP effect in the subwavelength scale faces challenges from both extremely weak signal detection and sample fabrication. Here, ultrafast optical spectroscopy is used to facilitate nonlinear optical signals detection[19−21] at a very weak level.[22,23] The FP interference is one of the icons of wave optics, which was discovered in 1899.[24] Most of the FP interference is considered for non-absorptive media at macroscopic scale. Although absorptive FP has also been considered, it is rarely applied to nanostructures. Here, we derive an absorptive FP equation that well explains our results in a metallic nanostructure.

Ultrafast femtosecond laser (Coherent Inc.) pulses with 830 nm central wavelength, 45 fs pulse width, and 80 MHz repetition rate are used. The experimental schematic setup is shown in Fig. 1(d). A series of metallic films of different thicknesses, with rectangular air-hole arrays, are carefully prepared. Gold thin films of different thicknesses (60 nm, 100 nm, 160 nm and 200 nm, respectively) are deposited onto BK7 glass substrates, where a 5-nm-thick Ti adhesion layer is used. This procedure for manufacturing sample costs

*Supported by the National Key Research and Development Program of China under Grant Nos 2017YFA0303603 and 2016YFA0300303, the National Natural Science Foundation of China under Grant Nos 11504062, 11774408 and 11574383, the Strategic Priority Research Program of Chinese Academy of Sciences under Grant No XDB30000000, the Chinese Academy of Sciences Interdisciplinary Innovation Team, and the External Cooperation Program of Chinese Academy of Sciences under Grant No GJHZ1826.

**Corresponding author. Email: jmzhao@iphy.ac.cn

great effort, because each time only a sample with one thickness can be made using electronic deposition. Rectangular arrays of 20×20 air holes with a periodicity of 410 nm are milled with focused ion beam (FIB) on these films with total area $8\,\mu m \times 8\,\mu m$. All air hole arrays have the same size with a length of $x = 260$ nm and a width of $y = 130$ nm (thus an aspect ratio of AR=$x/y = 2$). A scanning electron microscope (SEM) image of a typical hole array pattern on a 160-nm-thick Au film is shown in Fig. 1(a). The actual thickness of the Au film in the pattern area is characterized by an atomic force microscope (AFM), as shown in Fig. 1(b), note that the thickness includes that of a 5 nm Ti adhesion layer.

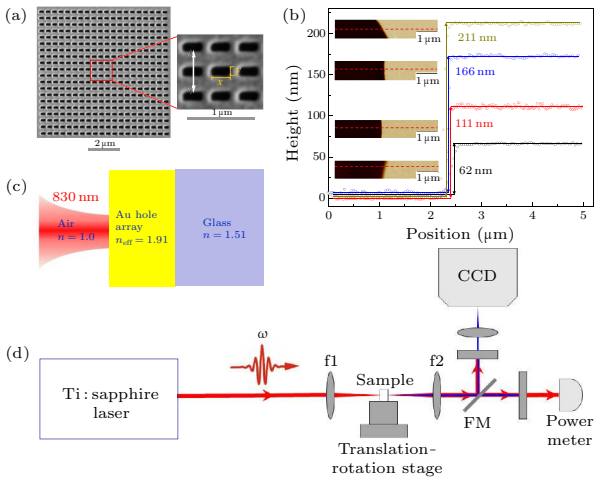

Fig. 1. (a) A SEM image of a typical sample of the rectangular hole array with the x–y direction and laser polarization (parallel to the y-axis) marked on the high resolution image, where AR=2. (b) The actual thickness measured by AFM. (c) Schematic diagram of the sample under light illumination. The refractive index of Au hole array is 1.91 and that of BK7 glass is 1.51. (d) Schematic experimental setup.

Under the condition of normal incidence, the laser beam is focused onto the sample with a lens of 50.8 mm focal length and has a diameter of about 30 μm on the front surface of sample. The transmitted fundamental wave and SHG signals are collected after the laser pulses pass through a lens with 63.5 mm focal length. The laser beam is linearly polarized vertical to the optical table, and the samples are mounted on a manual translation/rotation stage, which is aligned such that the y direction is always parallel to the laser polarization (see Fig. 1(a)). For the SHG measurement, the incident laser beam has an average power of 30 mW. The size of the pattern area is 8 μm and the diameter of spot size is 30 μm, so the efficient input power of pattern area is estimated to be about 10 mW, which generates very weak SHG signal during light propagation.

To observe the extremely weak SHG signal, a low-pass edge filter with a transmission of $T = 6 \times 10^{-9}$ for the fundamental beam and $T = 98\%$ for the SHG signal is used to sharply reduce the 830 nm pulses. Then the beam after the filter is focused onto a spectrometer (iHR 550 with photomultiplier tube and symphony CCD, JY Horiba Inc.). During the angle-resolved measurement, the angle ϕ between the laser beam (i.e., the z direction) and the x direction is tuned, where the sample is rotated and the incident laser beam stays unchanged. Because the subwavelength hole is much smaller than the light spot on the sample, this adjustment would not result in significant mismatch between the laser beam and the air hole. For different AR measurements, the sample is rotated 90° along the z direction, such that the AR=2 and AR=0.5 cases can be compared.

In Fig. 1(c) we plot the schematic sample structure, with the illustration of an 830 nm incident ultrafast laser beam. As is shown, the refractive index of BK7 glass is $n = 1.51$, and we estimate the effective refractive index of the gold thin film with holes at 830 nm wavelength to be $n_{\rm eff} = 1.91$.[25] Under the condition of normal incidence, the intensities of the linear transmission and the SHG signal vary with the metallic film thickness. For all of the thicknesses, both the linear transmission and the SHG signal of the AR=2 sample are much higher than those for the AR=0.5 sample, which is due to the already known shape resonance.[7,10] The fact that the SHG signal is $10^{-12} \sim 10^{-10}$ times weaker than the linear transmission[11] fulfills the non-depletion regime condition.

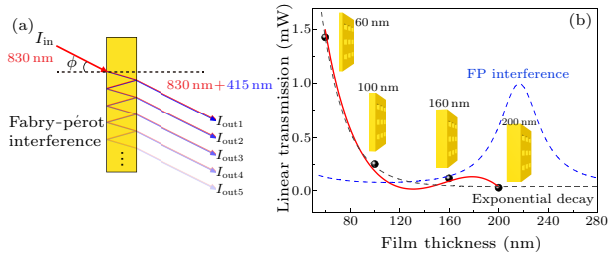

Fig. 2. (a) Illustration of the FP effect in the samples. The incident angle is ϕ. Both the linear (red line) and SHG (blue line) output beams are plotted. Light reflections within the sample is also depicted. (b) The linear transmission of the AR=0.5 samples with different thicknesses (60, 100, 160 and 200 nm). The black spheres are the experimental results. Correspondingly, the samples are illustrated explicitly as insets. The FP effect without absorption (normalized, blue dashed curve) and the evanescent exponential decay (gray dashed curve) are individually plotted. The FP effect considering the absorption fits the experimental results very well (red line).

We particularly analyze the linear transmission of AR=0.5, which is plotted in Fig. 2(b). We analyze the AR=0.5 case because by doing so we avoid the shape resonance known for the AR=2 case.[10] The AR=0.5 case possesses the property of a thin metallic film in general. If there is no FP interference, then the linear transmission overall will decay exponentially as the sample thickness increases, which is

a direct exhibition of the evanescent wave picture.[5] We fit this overall exponential decaying trend with $I(l) = A_0 \exp(-l/l_0)$, where A_0 is the amplitude, l is the thickness of sample, and l_0 is the skin depth (gray dashed curve in Fig. 2(b)). The fitting yields a skin depth of $l_0 = 20.0$ nm. It can be easily seen that a simple exponential decay does not fit well with our data at 160 nm.

As shown in Fig. 2(a), the multiple reflections of an incident light between the front and back surfaces will interfere with each other, which leads to a varying transmission that depends on the sample thickness, sample absorption, and angle of incidence. Because the exponential decay cannot fully explain our experimental observations, we consider the FP effect instead.

The original FP effect considers only the non-absorptive case. The linear transmissivity for a pure FP interference effect reads

$$T_{\text{non-absorptive}} = \frac{(1-R)^2}{1-2R\cos(\delta)+R^2} = \frac{1}{1+F\sin^2(\delta/2)}, \quad (1)$$

where $F = \frac{4R}{(1-R)^2}$ is the coefficient of finesse, R is the reflectivity of our sample, $\delta = 2\pi\Delta/\lambda$ is the phase difference, $\Delta = 2ln_{\text{eff}}\cos(\phi)$ is the optical path difference, l is the film thickness, and ϕ is the incident angle of light beam. By taking $\phi \approx 0°$, the normalized FP interference curve is explicitly plotted in Fig. 2(b) (blue dashed line). Given the effective refractive index $n_{\text{eff}} = 1.91$ obtained in Fig. 1(c), the effective wavelength within the sample is calculated to be $\lambda_{\text{eff}} = \lambda/n_{\text{eff}} = 435$ nm. Destructive interference occurs when the transmitted beams have a phase difference δ that is an odd multiple of π. Thus the beams destructively interfere within the thin film at $\lambda_{\text{eff}}/4 = 108.6$ nm.

Next we elucidate a more realistic case; i.e., the absorptive FP interference effect. Consider that the material sandwiched between its front and back surfaces is absorptive. The total linear transmissivity at the back surface is (see the supplemental material)

$$T_{\text{total}} = \frac{T^2\exp(-\frac{2\alpha l}{\cos\phi})}{1+R^2\exp(\frac{-4\alpha l}{\cos\phi})-2R\exp(\frac{-2\alpha l}{\cos\phi})\cos(\delta)} = \frac{1}{1+F'\sin^2(\delta/2)}, \quad (2)$$

where $F' = \frac{2e^{2\alpha l/\cos\phi}}{(1-\cos\delta)}\frac{(1-2Re^{2\alpha l/\cos\phi})^2}{T^2} - \frac{2}{1-\cos\delta} + \frac{4R}{T^2}$ is the coefficient of finesse, $\alpha = 0.00381/\text{nm}$ is the absorption coefficient, $R = \sqrt{R_1R_2} = 0.56$, $T = \sqrt{T_1T_2}$, $R_1(R_2)$ is the intensity reflectivity at the front (back) surface, and $T_1(T_2)$ is the intensity transmissivity at the front (back) surface. Under the normal incidence condition, we have $\phi = 0$ for the results shown in Fig. 2. It can be seen from Fig. 2(b) that the experimental results (black sphere) are very well-fitted by Eq. (2) (red line). Hence, the result in Fig. 2 directly verifies the existence of the FP interference in our metallic thin films. Compared with the non-absorptive FP case (blue-dashed curve), the absorption of the material prominently shifts the destructive interference thickness from 108.6 nm to 130 nm. Note that the FP mechanism does not lead to a diminished value for the transmission at 130 nm.

To further verify the FP mechanism, we investigate the angle dependence of the linear transmission and SHG signal for samples (AR=2) of different thicknesses (60 nm, 100 nm, 160 nm and 200 nm). We illustrate the schematic experimental setup in Fig. 3(a). The incident angle ϕ is varied by rotating the sample, and its effect on the linear and SHG signal intensities are recorded. Previous investigations have shown that the linear transmission sensitively depends on the incident angle.[1,9,12,15,26,27] These investigations only cover up to the $0° \leqslant \phi \leqslant 32°$ range. Here we explore a much larger range of incident angle, $0° \leqslant \phi \leqslant 53°$. Our results exhibit a similar trend for the linear transmission (Figs. 3(b)–3(e)). Overall, the intensity decreases as ϕ increases.

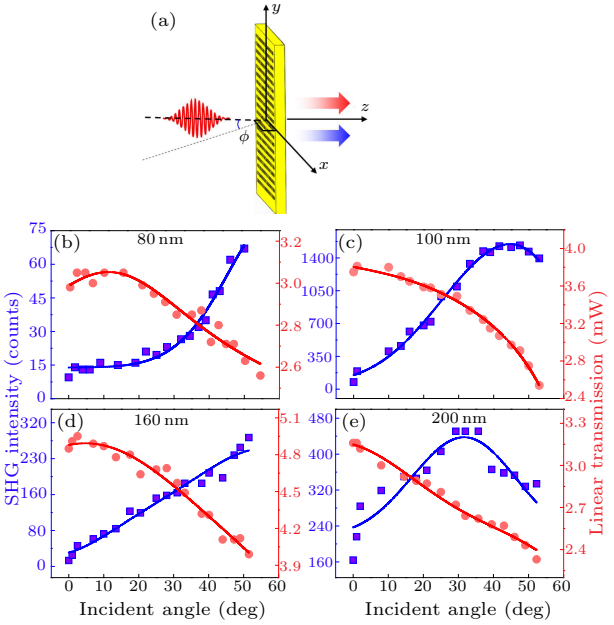

Fig. 3. (a) Schematic setup for the angle-resolved experiment. The samples are rotated, with the incident light unchanged. (b)–(e) The angle dependence of the linear transmission (red circle) and SHG intensity (purple square) for the AR=2 samples with thicknesses of 60 nm, 100 nm, 160 nm and 200 nm, respectively. The red curves are the fitting curves using Eq. (2) depicting the FP effect with absorption within samples of various thicknesses. The blue curves are the fitting results with $T^2_{\text{total}}\sin^2\phi\cos^4\phi$ depicting both the FP effect and the broken inversion symmetry.

Note that no previous studies have revealed the un-

derlying physics mechanism of the angle dependence. There are even no quantitatively investigations of the angle dependence. This is a challenging task that has been left untouched for a decade thanks to the obscure fundamental mechanism of the transmission itself. Here, we thoroughly investigate this phenomenon and aim to uncover the underlying mechanism. We fit the measured data shown in Figs. 3(b)–3(e) by Eq. (2) that we derive based on the FP effect for absorptive materials. It can be seen that the experimental results can be fitted very well ([Figs. 3(b)–3(e), red curves). This fitting is not a pure mathematical fitting, rather, it is a direct derivation of the absorptive FP interference effect (Eq. (2)). Therefore, the experimental and theoretical results in Fig. 3 together significantly confirm the absorptive FP mechanism discussed above (see Fig. 2).

Moreover, since we have demonstrated the FP interference of the linear transmission, it is conceivable that this effect will be reflected in its SHG signal. The SHG intensity, which is in a quadratic relation with the linear transmission $I_{\rm SHG} \propto T_{\rm total}^2$, will experience an intensity variation accordingly. Further, it was shown half a century ago[28] that in a metallic material, the reflective SHG, by omitting higher order terms, has an extra intensity dependence on the incident angle, $I_{\rm SHG} \propto \sin^2\phi\cos^4\phi$, which is due to the broken inversion symmetry. We expect that the transmission SHG shares the same property. Therefore, we expect to have

$$I_{\rm SHG} \propto T_{\rm total}^2 \sin^2\phi\cos^4\phi. \tag{3}$$

To verify this, we measure the angle dependence of the SHG intensity for all the samples of different thicknesses. An AR=2 configuration is implemented to ensure that the SHG signal is strong enough to detect. Because there is a fixed ratio between the SHG intensity of different ARs,[10] this configuration also reflects the results of the regular AR=0.5 configuration. The results are shown in Figs. 3(b)–3(e), which demonstrate at a first glance drastically different angle dependences. We fit this seemingly very complex dependence property. We use Eq. (3) to fit all our SHG experimental results shown in Fig. 3. It can be seen that our theoretical curves (blue curves in Fig. 3) all fit very well the experimental SHG data. The drastically different dependence (Figs. 3(b)–3(e)) arises because the term $T_{\rm total}$ is also a function of ϕ, i.e., $T_{\rm total}(\phi)$, which also depends on the sample thickness. The surprisingly good comparison between the experimental SHG signal and the fitting based on Eq. (3) demonstrates explicitly the clear FP interference effect on the SHG. We note that the SHG data (blue curve) in Fig. 3 is a double-confirmation of the linear transmission data (red curve) in Fig. 3. Indeed, these two groups of experimental results are equally strong evidences of the FP interference effect. Consequently, our experiment of the angle-dependent SHG signal again quantitatively confirms the existence of FP effect in a thin absorptive metallic film or nanostructure.

In Fig. 3(e), there are some discrepancies that we attribute to data fluctuation. The reason why the data fluctuation for the 200 nm sample is relatively larger is that the thicker sample has a more sensitive dependence on angle. This happens because for a thicker sample: for the situation of a small angle, the light beam experiences the metallic wall of the hole/channel more prominently than through a thinner sample; for the situation of a larger angle, the light beam experiences the wall reflections earlier (upon increasing the angle) than through a thinner sample. As shown in Figs. 3(d) and 3(e), the data fluctuations are mainly located at the small angles and large angles, respectively.

Finally, we consider potential applications of the absorptive FP effect in the subwavelength nanostructure. It has been shown recently that optical absorption and emission in atomically thin two-dimensional (2D) materials can be enhanced via modulating a spacer's thickness in an FP cavity,[29–32] which leads to enhanced constructive resonance, and hence device performance.[32] However, this relies on the insertion of a spacer into the cavity, which hampers the scaling of device fabrication. Here, our direct observation of the absorptive FP effect in metallic nanostructure makes it possible to realize the FP effects by tuning the cavity thickness, rather than using a spacer. Thus, our findings have potential applications in scalable optoelectronic devices based on 2D materials.

In summary, we have experimentally demonstrated the existence of the FP effect in a series of Au thin films with thickness less than the wavelength. In our experiment, the thickness dependence of linear transmission demonstrates the existence of absorptive FP interference, and the angle dependence of both the linear and SHG signals further verifies the absorptive FP effect. Our finding has potential applications in tuning the performance of nano-photonics devices containing metallic nanostructures.

References

[1] Ebbesen T W, Lezec H J, Ghaemi H F, Thio T and Wolff P A 1998 *Nature* **391** 667
[2] Koerkamp K J K, Enoch S, Segerink F B, van Hulst N F and Kuipers L 2004 *Phys. Rev. Lett.* **92** 183901
[3] Gordon R, Brolo A G, McKinnon A, Rajora A, Leathem B and Kavanagh K L 2004 *Phys. Rev. Lett.* **92** 037401
[4] Degiron A and Ebbesen T W 2005 *J. Opt. A: Pure Appl. Opt.* **7** S90
[5] Degiron A, Lezec H J, Barnes W L and Ebbesen T W 2002 *Appl. Phys. Lett.* **81** 4327
[6] Martin-Moreno L, Garcia-Vidal F J, Lezec H J, Pellerin K M, Thio T, Pendry J B and Ebbesen T W 2001 *Phys. Rev.*

Lett. **86** 1114
[7] van Nieuwstadt J A, Sandtke M, Harmsen R H, Segerink F B, Prangsma J C, Enoch S and Kuipers L 2006 *Phys. Rev. Lett.* **97** 146102
[8] Lesuffleur A, Kumar L K S and Gordon R 2007 *Phys. Rev. B* **75** 045423
[9] Lesuffleur A, Kumar L K S and Gordon R 2006 *Appl. Phys. Lett.* **88** 261104
[10] Wang B L, Wang R, Liu R J, Lu X H, Zhao J and Li Z Y 2013 *Sci. Rep.* **3** 2358
[11] Bao Y J, Peng R W, Shu D J, Wang M, Lu X, Shao J, Lu W and Ming N B 2008 *Phys. Rev. Lett.* **101** 087401
[12] van der Molen K L, Klein K J, Enoch S, Segerink F B, van Hulst N F and Kuipers L 2005 *Phys. Rev. B* **72** 045421
[13] Takakura Y 2001 *Phys. Rev. Lett.* **86** 5601
[14] Yang F and Sambles J R 2002 *Phys. Rev. Lett.* **89** 063901
[15] Cao Q and Lalanne P 2002 *Phys. Rev. Lett.* **88** 057403
[16] Wei H, Pan D, Zhang S P, Li Z P, Li Q, Liu N, Wang W H and Xu H X 2018 *Chem. Rev.* **118** 2882
[17] Wei H, Zhang S P, Tian X R and Xu H X 2013 *Proc. Natl. Acad. Sci. USA* **110** 4494
[18] Gao F, Li D, Peng R W, Hu Q, Wei K, Wang Q J, Zhu Y Y and Wang M 2009 *Appl. Phys. Lett.* **95** 011104
[19] Wu Y, Wu Q, Sun F, Cheng C, Meng S and Zhao J 2015 *Proc. Natl. Acad. Sci. USA* **112** 11800
[20] Wu R, Zhang Y, Yan S, Bian F, Wang W, Bai X, Lu X, Zhao J and Wang E 2011 *Nano Lett.* **11** 5159
[21] Sun F, Wu Q, Wu Y L, Zhao H, Yi C J, Tian Y C, Liu H W, Shi Y G, Ding H, Dai X, Richard P and Zhao J M 2017 *Phys. Rev. B* **95** 235108
[22] Tian Y C, Zhang W H, Li F S, Wu Y L, Wu Q, Sun F, Zhou G Y, Wang L L, Ma X C, Xue Q K and Zhao J M 2016 *Phys. Rev. Lett.* **116** 107001
[23] Zhao J, Bragas A V, Lockwood D J and Merlin R 2004 *Phys. Rev. Lett.* **93** 107203
[24] Fabry C and Pérot A 1899 *Amm. Chim. Phys.* **16** 7
[25] Verhagen E, Spasenovic M, Polman A and Kuipers L K 2009 *Phys. Rev. Lett.* **102** 203904
[26] Bravo-Abad J, Degiron A, Przybilla F, Genet C, García-Vidal F J, Martín-Moreno L and Ebbesen T W 2006 *Nat. Phys.* **2** 120
[27] Gompf B, Braun J, Weiss T, Giessen H, Dressel M and Hubner U 2011 *Phys. Rev. Lett.* **106** 185501
[28] Bloembergen N, Chang R K, Jha S S and Lee C H 1968 *Phys. Rev.* **174** 813
[29] Liu J T, Wang T B, Li X J and Liu N H 2014 *J. Appl. Phys.* **115** 193511
[30] Lien D H, Kang J S, Aamani M, Chen K, Tosun M, Wang H P, Roy T, Eggleston M S, Wu M C, Dubey M, Lee S C, He J H and Javey A 2015 *Nano Lett.* **15** 1356
[31] Jeong H Y, Kim U J, Kim H, Han G H, Lee H, Kim M S, Jin Y, Ly T H, Lee S Y, Roh Y G, Joo W J, Hwang S W, Part Y and Lee Y H 2016 *ACS Nano* **10** 8192
[32] Wang Q X, Guo J, Ding Z J, Qi D Y, Jiang J Z, Wang Z, Chen W, Xiang Y J, Zhang W J and Wee A T S 2017 *Nano Lett.* **17** 7593

Supplementary Materials: Absorptive Fabry-Pérot Interference in a Metallic Nanostructure

Rui Wang(王瑞)[1], Y. L. Wu(吴艳玲)[2], B. H. Yu(余博晗)[2,3], L. L. Hu(胡立立)[2], C. Z. Gu(顾长志)[2,3], J. J. Li(李俊杰)[2,3], Jimin Zhao(赵继民)[2,3,4]*

[1] CAS Key Laboratory of Standardization and Measurement for Nanotechnology, CAS Center for Excellence in Nanoscience, National Center for Nanoscience and Technology, Beijing 100190
[2] Beijing National Laboratory for Condensed Matter Physics, Institute of Physics, Chinese Academy of Sciences, Beijing 100190
[3] School of Physical Sciences, University of Chinese Academy of Sciences, Beijing 100049
[4] Songshan Lake Materials Laboratory, Dongguan 523808

*Corresponding author, Email: jmzhao@iphy.ac.cn

The following derivation is based on the illustration in Fig. S1. As light incident on the FP etalon, T_0 is transmitted through the etalon, T_1 is transmitted after twice extra reflections. At each surface, the reflectivity of the field is taken to be $\sqrt{R}$, and the transmission of the field is $\sqrt{T}$. We denote the refractive index inside the etalon by n, and that outside by n_0, with $n > n_0$.

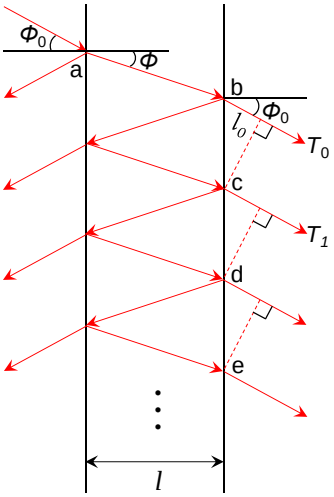

Fig. S1. The schematic of FP interference effect.

We take the incident amplitude at point a (outside of the etalon) to be 1. Considering the phase change of the electromagnetic wave due to the light propagation within the etalon, the transmitted beam at point b (outside of the etalon) has a field amplitude of

$$t_0 = \sqrt{T_1}e^{-\alpha l/\cos\Phi}\sqrt{T_2}e^{ikl/\cos\Phi} = \sqrt{T_1T_2}e^{-\alpha l/\cos\Phi}e^{ikl/\cos\Phi} \quad , \tag{4}$$

where $k = 2\pi n/\lambda$, T_1 and T_2 are the intensity transmissivity of the front surface and back surface, respectively; R_1 and R_2 are intensity reflectivity of the front surface and back surface, respectively. At point c (outside of the etalon), the transmitted amplitude is

$$t_1^{'} = \sqrt{T_1}e^{-\alpha l/\cos\Phi}\sqrt{R_2}e^{-\alpha l/\cos\Phi}\sqrt{R_1}e^{-\alpha l/\cos\Phi}\sqrt{T_2}e^{3ikl/\cos\Phi} = \sqrt{T_1T_2}\sqrt{R_1R_2}e^{-3\alpha l/\cos\Phi}e^{3ikl/\cos\Phi}. \tag{5}$$

When obtaining the sum of the amplitude of the transmitted beams, the phase different should be considered. The amplitude $t_1^{'}$ is retarded relative to t_0 in phase by an amount of k_0l_0, where $k_0 = 2\pi n_0/\lambda$, $l_0 = 2l\mathrm{tg}\Phi\sin\Phi_0$. For

$$t_1 = t_1^{'}e^{-ik_0l_0} = \sqrt{T_1T_2}\sqrt{R_1R_2}e^{-3\alpha l/\cos\Phi}e^{3ikl/\cos\Phi}e^{-ik_0l_0}. \tag{6}$$

the phase difference between the two beams t_0 and t_1 is

$$\frac{2kl}{\cos\Phi} - k_0l_0 = 2kl\cos\Phi = \delta. \tag{7}$$

To within a constant multiplicative phase factor (*i.e.*, ignore $e^{ikl/cos\Phi}$), the amplitude of the m^{th} transmitted can be written as

$$t_m = \sqrt{T_1T_2}(\sqrt{R_1R_2})^m e^{-(2m+1)\alpha l/\cos\Phi}e^{(2m+1)ikl/\cos\Phi}e^{-imk_0l_0}. \tag{8}$$

Thus, the total transmitted amplitude is the sum of the all individual beams' amplitudes:

$$\begin{aligned} t = \sum_{m=0}^{\infty} t_m &= \sqrt{T_1T_2}\sum_{m=0}^{\infty}(\sqrt{R_1R_2})^m e^{-(2m+1)\alpha l/\cos\Phi}e^{im\delta} \\ &= \sqrt{T_1T_2}e^{-\alpha l/\cos\Phi}\sum_{m=0}^{\infty}(\sqrt{R_1R_2})^m e^{(-2\alpha l/\cos\Phi+i\delta)m}. \end{aligned} \tag{9}$$

As $\dfrac{1}{1\text{-}Z} = 1+Z+Z^2+\cdots+Z^n+\cdots = \sum_{n=0}^{\infty} Z^n \quad (|Z|<1)$, we have

$$\begin{aligned} t &= \sqrt{T_1T_2}e^{-\alpha l/\cos\Phi}\frac{1}{1-\sqrt{R_1R_2}e^{-2\alpha l/\cos\Phi}e^{i\delta}} \\ &= \frac{\sqrt{T_1T_2}e^{-\alpha l/\cos\Phi}}{[(1-\sqrt{R_1R_2}e^{-2\alpha l/\cos\Phi}\cos\delta) - i\sqrt{R_1R_2}e^{-2\alpha l/\cos\Phi}\sin\delta]}. \end{aligned} \tag{10}$$

By defining $x = 1-\sqrt{R_1R_2}e^{-2\alpha l/\cos\Phi}\cos\delta$ and $y = \sqrt{R_1R_2}e^{-2\alpha l/\cos\Phi}\sin\delta$, so

$$\begin{aligned} t &= \frac{\sqrt{T_1T_2}e^{-\alpha l/\cos\Phi}}{x-iy} = \frac{\sqrt{T_1T_2}e^{-\alpha l/\cos\Phi}(x+iy)}{x^2+y^2}, \\ t^* &= \frac{\sqrt{T_1T_2}e^{-\alpha l/\cos\Phi}(x-iy)}{x^2+y^2}. \end{aligned} \tag{11}$$

Thus, we obtain the normalized transmission $T_{absorptive}$ as

$$\begin{aligned} T_{absorptive} = tt^* &= \frac{\sqrt{T_1T_2}e^{-\alpha l/\cos\Phi}(x+iy)}{x^2+y^2}\cdot\frac{\sqrt{T_1T_2}e^{-\alpha l/\cos\Phi}(x-iy)}{x^2+y^2} \\ &= \frac{\sqrt{T_1T_2}e^{-2\alpha l/\cos\Phi}}{1-2\sqrt{R_1R_2}e^{-2\alpha l/\cos\Phi}\cos\delta + R_1R_2e^{-4\alpha l/\cos\Phi}}, \end{aligned} \tag{12}$$

with $R_1+T_1=1$, $R_2+T_2=1$.